Applied Catalysis B: Environmental 251 (2019) 49–56

Contents lists available at ScienceDirect

Applied Catalysis B: Environmental

journal homepage: www.elsevier.com/locate/apcatb

Facile synthesis of bimetallic Pt-Pd symmetry-broken concave nanocubes and their enhanced activity toward oxygen reduction reaction

Rifeng Wu[a], Panagiotis Tsiakaras[b,c,d,*], Pei Kang Shen[a,*]

[a] Collaborative Innovation Center of Sustainable Energy Materials, Guangxi Key Laboratory of Electrochemical Energy Materials, State Key Laboratory of Processing for Non-ferrous Metal and Featured Materials, Guangxi University, Nanning, 530004, PR China
[b] Laboratory of Electrochemical Devices based on Solid Oxide Proton Electrolytes, Institute of High Temperature Electrochemistry, RAS, Yekaterinburg, 620990, Russia
[c] Laboratory of Materials and Devices for Clean Energy, Ural Federal University, 19 Mira Str., Yekaterinburg, 620002, Russia
[d] Laboratory of Alternative Energy Conversion Systems, Department of Mechanical Engineering, School of Engineering, University of Thessaly, Pedion Areos, 38834, Greece

ARTICLE INFO

Keywords:
Pt-Pd bimetallic catalysts
Symmetry-broken concave cubes
High-index facets
Pt-rich surface
Oxygen reduction reaction

ABSTRACT

In the present work, we are reporting a facile one-pot synthesis route to get Pt-Pd symmetry-broken concave nanocube (SBCNCs) structures in *N*, *N*-dimethylformamide (DMF) solutions under the effect of iodide ions and Poly (vinylpyrrolidone) (PVP). By given the inhibiting effect of non-stirring during the reaction process, and the capping agent effect, newly formed atoms is expected to accumulate at the vertexes and/or the edges of nanocube, leading to the formation the Pt-Pd SBCNCs. These structures are in a thorough manner physico-chemically and electrochemically characterized.

It is found that the specific structure of Pt-Pd SBCNCs is composed of various high-index facets and Pt-rich surface. These features enable a superior performance for the oxygen reduction reaction, and the specific/mass activities of the Pt-Pd SBCNCs are 7.7/6.2 times higher than commercial TKK-Pt/C, respectively. It also exhibits a remarkable durability by only reduced 30 mV half-wave potential after 15,000 accelerated durability test (ADT) cycles. This work provides an effective and simple strategy to rationally design electrocatalysts with enhanced activity and durability toward oxygen reduction reaction or other practical applications.

1. Introduction

Proton exchange membrane fuel cells (PEMFCs), as clean and efficient energy conversion electrochemical devices, present an increasing attraction over the past three decades [1–4]. However, high cost and poor durability of commercial Pt/C monometallic catalyst extremely restrict the commercialization of PEMFCs. As far as we know, Pt-based catalysts are among the most promising ones with good catalytic performance. Great efforts have been done toward the synthesis of Pt-based alloy catalysts, such as bimetallic Pt-Ni [5], Pt-Co [6], Pt-Cu [7], Pt-Pd [8] and multi-metallic Pt-Pd-X (X = Cu, Ni [9,10], which decrease Pt usage, enhancing simultaneously the electrocatalytic performance. Owing to the same face-centered cubic structure and nearly the same lattice constant (lattice mismatch of 0.77%), Pt and Pd easily form bimetallic alloy structure. Contrary to other metals (such as Cu, Co or Ni), Pd itself exhibits a high catalytic performance in many industrial applications, and high stability under harsh reaction conditions [11]. In conclusion, over the past few decades, tremendous research has been made towards the facile and cost-effective synthesis of Pt-Pd nanostructured catalysts with specific shapes or morphologies, such as nanotubes, concave cubes, hollow structures, nanodendrites, nanoflowers, and so on [12–16]. The catalytic performance of nanocrystals in a large extent depends on its structure and morphology, especially when the high-index facet is exposed on the surface [17–19]. However, it is still difficult to prepare such geometrically complex and thermodynamically unfavorable structures with one-pot synthesis methods. The recipe most frequently reported in the paper was based on seed-mediated growth with two or more steps [20,21]. Zhang and co-workers produced Pd-Pt bimetallic concave structure through a two-step synthesis method. Firstly, bromine ion was used as a capping agent for the (100) crystal facet to synthesize Pd nanocube; Subsequently, the supernatant and the Pt precursor were mixed, to get Pt-Pd concave nanocube via galvanic replacement [13].

Herein, we are introducing a rationally designed protocol for the one-pot synthesis of symmetry-broken concave nanocube. In a standard synthesis of Pt-Pd SBCNCs, disodium tetrachloropalladate (Na_2PdCl_4), chloroplatinic acid hexahydrate (H_2PtCl_6 $6H_2O$) and sodium iodide (NaI) were mixed with DMF (see the experimental section for details). The resulting homogeneous solution was then transferred into a 25 mL Teflon-lined stainless-steel autoclave. After that, the sealed vessel was

* Corresponding authors.
E-mail addresses: pkshen@gxu.edu.cn (P.K. Shen), tsiak@mie.uth.gr (P. Tsiakaras).

https://doi.org/10.1016/j.apcatb.2019.03.045
Received 19 November 2018; Received in revised form 12 March 2019; Accepted 16 March 2019
Available online 18 March 2019
0926-3373/

heated at 130 ℃ for 5 h in an air-dry oven without stirring. Noticeably, this method for the Pt-Pd CNCs preparation with both metal precursors simultaneously presented in the reaction solution, which is quite different from the seed-mediated method and the traditional methods [13,22–26]. It is hard to reduce Pd (II) before Pt (IV) when they are under the same conditions, because of the standard reduction potentials (E°) between Pd^{2+}/Pd and Pt^{4+}/Pt. However, owing to the effect of iodide ions [27], and several Pt (IV) species due to the aqua and hydroxo substitution for $PtCl_6^{2-}$ complex in an aqueous solution [28,29], Pd precursors will preferentially be reduced over Pt precursors. At the effect of facet-selective (100) capping agent of I^-, Pt-Pd nanocube will be obtained at the initial stage. The sluggish surface diffusion rates, since without stirring, will lead to directional growth along the vertexes and pile-up of new atoms at the corner of the cubes, and the formation of asymmetry concave nanocubes [30].

In the present work, it is reported a simple and cost-effective method to prepare Pt-Pd bimetal symmetry-broken concave nanocube catalysts with superior electrochemical oxygen reduction performance.

2. Experimental

2.1. Chemical and materials

All reagents were of analytical grade and used as received without any further purification. More precisely, chloroplatinic acid hexahydrate ($H_2PtCl_6{\cdot}6H_2O$ ≥37.0%) and palladium chloride ($PdCl_2$ ≥99%) were purchased from Changshu Changhong precious metal Co. Ltd (Jiangsu, China). Na_2PdCl_4 solution is prepared by dissolving $PdCl_2$ in NaCl solution. N, N-dimethylformamide (DMF, 99.9%), Poly(vinylpyrrolidone) (PVP, MW≈55,000), sodium iodide (NaI, AR, 99.5%), perchloric acid ($HClO_4$, GR, 70.0–72%), n-butylamine and sodium chloride (NaCl, AR, 99.5%) were purchased from Macklin Regent. Acetone and ethanol were purchased from Tianjin Damao. The commercial carbon black Vulcan XC-72R was supplied from Cabot Inc. The water used in all experiments was ultrapure (18.2 MΩ).

2.2. Synthesis of Pt-Pd bimetallic nanostructures

In a typical synthesis of Pt-Pd SBCNCs, 0.15 mmol Na_2PdCl_4 and 0.05 mmol $H_2PtCl_6{\cdot}6H_2O$ [sodium chloropalladate (aqueous solution of Na_2PdCl_4) and chloroplatinic acid hexahydrate (aqueous solution of $H_2PtCl_6.6H_2O$) in a molar ratio of 3:1] were subsequently injected into 10 mL N, N-dimethylformamide (DMF) solution in presence of 50 mg Poly(vinylpyrrolidone) (PVP) and 40 mg sodium iodide (NaI). The resulting homogeneous solution was transferred into a 25 mL teflon-lined stainless-steel autoclave, and ultrasonicated for 10 min. Then, the sealed vessel was heated at 130 ℃ for 5 h in an air-dry oven without stirring. After naturally cooling down to room temperature, the resulting colloidal product was washed (four times) and collected with ethanol/acetone mixture by centrifugation (at 8000 rpm). The Pt-Pd NCs are prepared with the standard procedure except that replace NaI with same molar amount NaBr, and keep other conditions unchanged.

2.3. Preparation of carbon-supported catalysts

In a typical preparation, the synthesized Pt-Pd bimetallic catalysts (5 mL of products) and 15 mg commercial carbon (Vulcan-72) were dispersed in 20 mL cyclohexane. The resultant mixture was ultrasonicated for 2 h at room temperature. After that, the as prepared materials were centrifuged with ethanol (three times) and then were dispersed in n-hexane. Afterwards, the precipitates were furtherly purified by absolute ethyl alcohol and were dried at 80 ℃ for 12 h. Before used as electrocatalysts, the as prepared samples were placed in a furnace and heated at 200 ℃ for 1 h in air. Finally, the samples were naturally cooled down to room temperature.

2.4. Materials characterizations

Transmission electron microscopy (TEM), High resolution-TEM (HRTEM), high angle annular dark field scanning transmission electron microscope (HAADF-STEM) characterizations were performed on a TITAN G2 (FEI, American) microscope at 300 kV. Powder X-ray diffraction (XRD) measurements were carried out on a Smart Lab 3 X-ray diffractometer (Rigaku Co, Japan), with Cu Kα radiation (λ = 1.5405 Å) at 40 kV and 30 mA. The 2θ angular regions between 20˚and 90˚were finely scanned at 5˚min^{-1} to analyze the chemical composition and lattice parameters of the samples. X-ray photoelectron spectroscopy (XPS) measurements were performed using an ESCALAB 250 Xi (Thermo Fisher Scientific, USA) spectrometer with an Al X-ray source operated at 150 W. Survey spectra were collected at a pass energy of 100.0 eV over the binding energy range of 0–1350 e V. The loadings of catalysts were determined by the inductively coupled plasma atomic emission spectroscopy (TJA RADIAL IRIS 1000 ICP-AES, USA).

2.5. Electrochemical measurements

Glassy carbon (GC) disk electrode (0.196 cm^{-2} in a geometric area) served as the substrate for the support, and it was polished using aqueous alumina suspension prior to use. Weighed 2 mg of the dried catalyst and dispersed in 2 ml 0.05 wt. % Nafion solution, followed by ultrasonication for 35 min. Finally, using a micropipette, 10 μl of the catalytic suspension was pipetted onto the pre-cleaned glassy carbon rotating disk electrode (RDE) and spin dry at 700 rpm to form a uniform thin film that was further characterized in the electrochemical cell. The Pt loading for all Pt-Pd nanocrystal electrocatalysts was controlled to be around 12.0 μg cm^{-2}, based on the geometric electrode area of 0.196 cm^2 determined by ICP-MS. For comparison, 2.0 mg of the commercial Pt/C catalyst (TKK, 46.7 wt % Pt, Japan) were mixed in 2 ml 0.05 wt % Nafion solution and 10 μl of this suspension were pipetted onto the GC surface and further characterized; the Pt loading was calculated as 23.83 μg cm^{-2}.

The electrochemical measurements were conducted in a three-compartment electrochemical cell with a Pine rotational disk electrode setup connected with a bipotentiostat (AFCBP1E, Pine Instrument Co., USA). A GC covered with catalyst, acted as the working electrode, a Pt mesh as the counter, and a reversible hydrogen electrode (RHE) as the reference electrode. The CV curve was recorded at 25 ℃ in a N_2-saturated 0.1 M $HClO_4$ solution in the potential range between 0.05–1.1 V RHE at a scanning rate of 50 mV s^{-1}. ORR measurements were conducted in O_2-saturated 0.1 M $HClO_4$ aqueous solution, and the ORR polarization curves were collected at 1600 rpm with scan rate of 10 mV s^{-1}. The accelerated durability tests (ADTs) were performed at 25℃ in O_2-saturated 0.1 M $HClO_4$ aqueous solutions by applying cyclic potential sweeps between 0.6 and 1.1 V versus RHE at a sweep rate of 100 m V s^{-1}. The ORR data were corrected by ohmic iR-drop compensation.

3. Results and discussion

The representative transmission electron microscopy (TEM) and high-angle annular dark-field scanning transmission electron microscopy (HAADF-STEM) images of Pt-Pd SBCNCs prepared using the standard procedure are shown in Fig. 1.

From the bright-field TEM and HAADF-STEM images in Figs. 1a 1b and 1c most of the nanocrystals present a typical symmetry-broken concave nanocube structure with a uniform distribution and an edge length of 16.6 ± 2.4 nm (Fig. S1). Fig. 1d show a High-resolution TEM (HRTEM) image of a single Pt-Pd SBCNCs oriented along the [001] zone axis (Fig. 1d). In addition, the angles between the facets of the projected symmetry-broken concave nanocube and the {100} facets of an ideal cube were determined to be α = 7.5˚, 9.6˚ and 10.2˚ ({610}), 12.5˚ ({510}), 15.9˚ ({720}), and 20.1˚ ({830}) (Fig. S2) [31–33]. The lattice

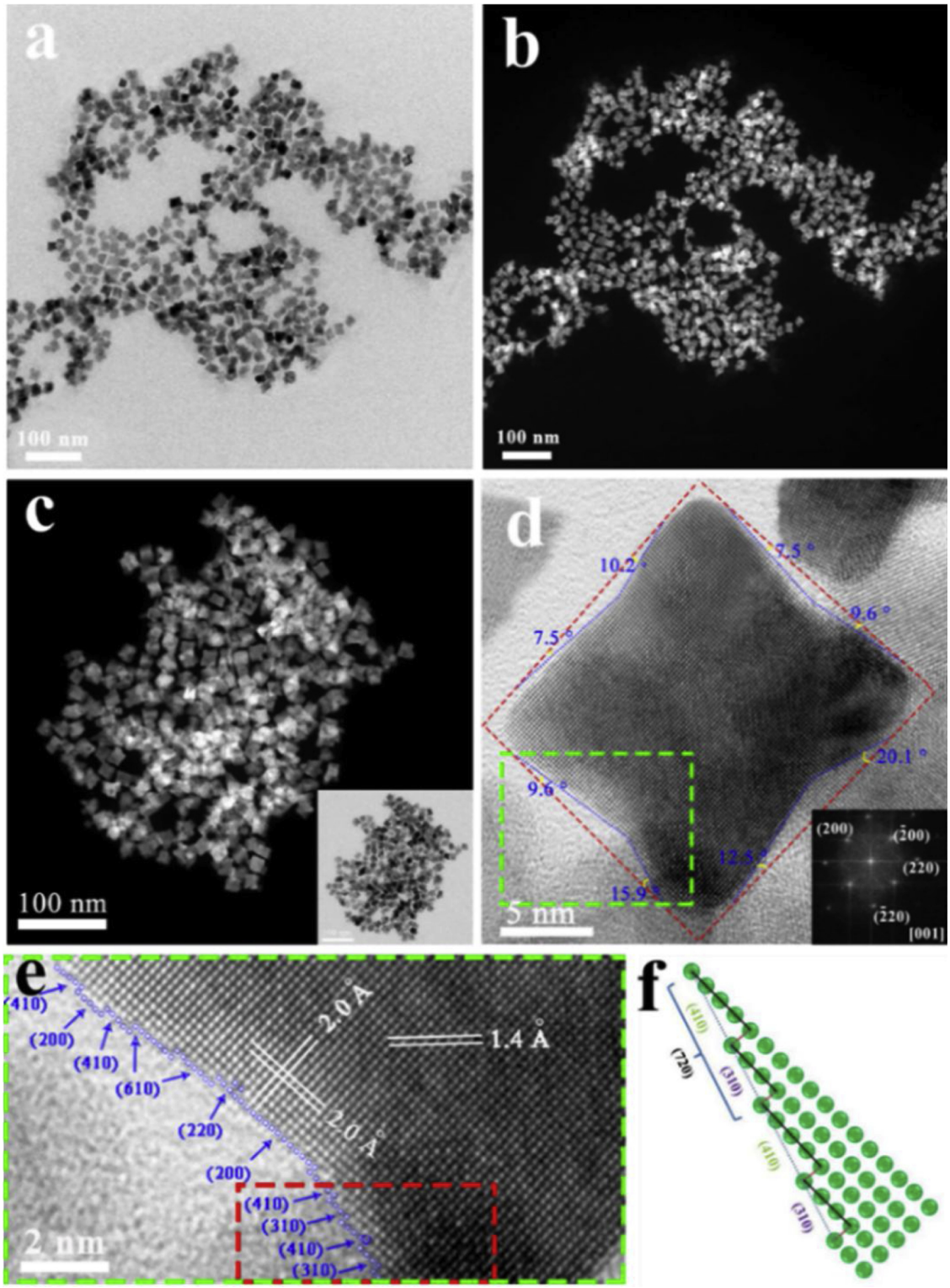

Fig. 1. (a) The typical low-magnification bright-field TEM, (b) and (c) low and medium-resolution HAADF-STEM image of the Pt-Pd symmetry-broken concave nanocubes (Pt-Pd SBCNCs), (d) TEM image of individual Pt-Pd SBCNCs, (e) High-resolution TEM image taken from the dotted square of (c), (f) Atomic model of Pt-Pd (720) plane with high density of steeped surface atoms.

fringes with an interplanar spacing of 0.20 and 0.14 nm, corresponding to the (200) and (220) planes of a face-centered cubic (fcc) lattice, respectively (Fig. 1e), which, further confirmed that the side surface of the concave region is likely bounded by a mix of both {100} and {110} facets) [13]. More importantly, abundant atomic steps and terrace are clearly observed at the concaves of the edge. According analysis, the steeped surface is enclosed by high-index facets with (100) terraces and (110) steps, such as (210), (310), (410), (610) and (720). Such a high-index facet is actually a periodical combination well consistent with the atomic model (Fig. 1f).

Detailed characterization of the elemental composition and distribution was carried out with EDS line scan profiles and elemental mapping (Fig. 2a). As shown in micrographs 2a_I and 2a_{II}, Pd is mainly distributed in the central core area, whereas Pt is enriched on the

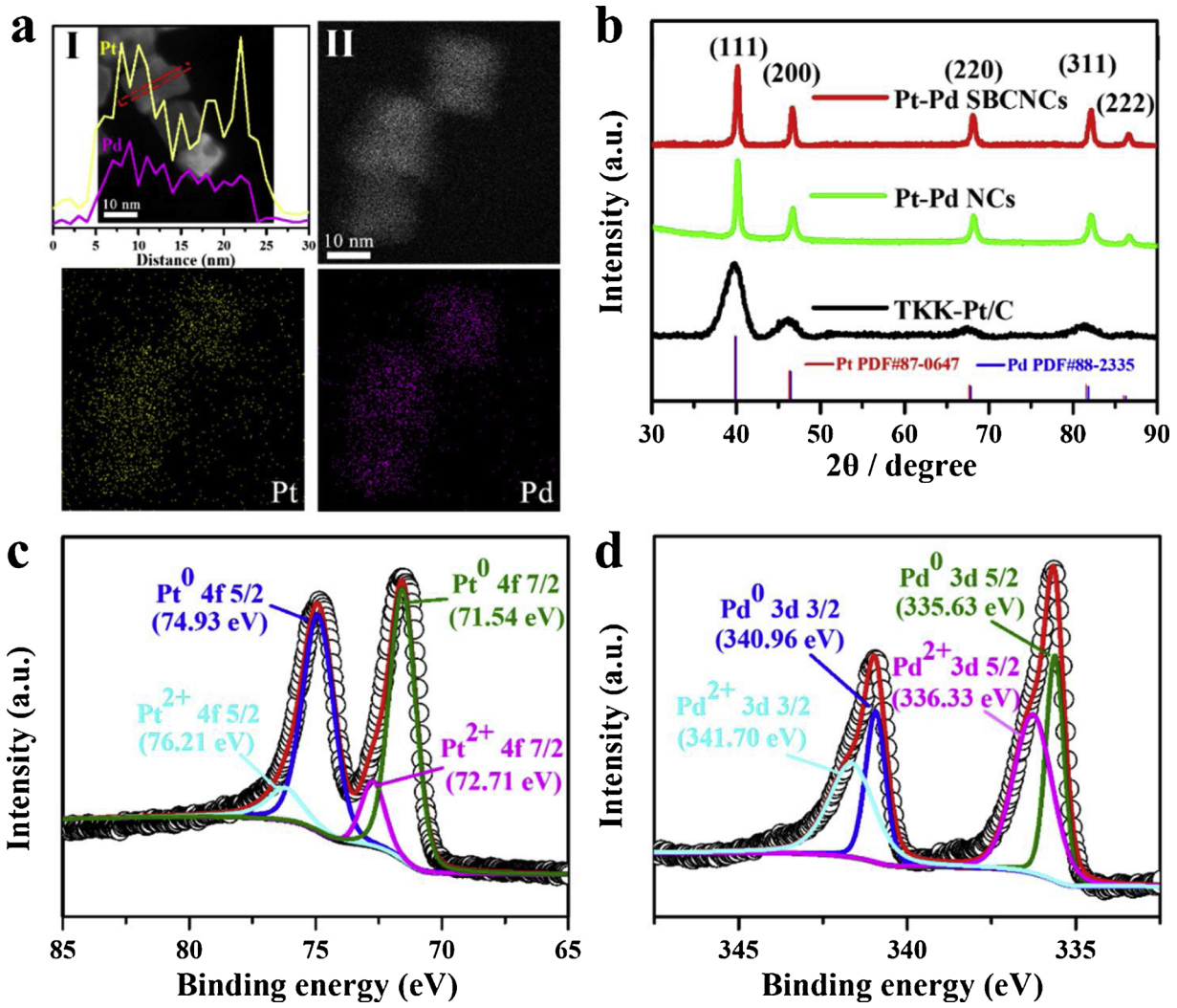

Fig. 2. (a_I) EDS line scan profiles of a single Pt-Pd SBCNC and (a_{II}) HAADF-STEM image and corresponding elemental mapping; (b) XRD patterns of commercial TKK-Pt/C, Pt-Pd NC and Pt-Pd SBCNC, at a scan rate of 10°min^{-1}; (c), (d) XPS pattern for the Pt 4f region and Pd 3d region of Pt-Pd SBCNC.

external surface, indicated a Pt-rich surface of core-shell structure. The overall Pt/Pd atomic ratio is 32.4:67.6, as determined by EDS analysis (Fig. S1), which is in good agreement with the inductively coupled plasma atomic emission spectrometry (ICP-MS) measurement. Fig. 2b shows the wide-angle XRD patterns of the typical Pt-Pd SBCNCs/C, Pt-Pd NCs/C and commercial TKK-Pt/C catalysts. It was very difficult to resolve Pt and Pd peaks in the XRD pattern, because the Pt/Pd lattice match ratio was 99.23%. The positions of diffraction peak can be clearly indexed to {111}, {200}, {220}, {311} and {222} diffractions of face-centered-cubic (fcc) structure type (Pt PDF#87-0647 and Pd PDF#88-2335). Compared with commercial Pt/C, there are slight shifts of peak positions to higher angles of Pt-Pd SBCNCs and Pt-Pd NCs, which confirm the formation of Pt-Pd alloy. XPS was used to determine the surface chemical state and elemental composition of the nanostructure. The XPS patterns show that both Pt and Pd are mainly of zero valence state on the nanocrystal surface (Figs 2c and 2d).

The Pt 4f binding energy (BE) values of the Pt–Pd SBCNCs positive shifts compared to commercial Pt/C (Fig. S3), are summarized in the Table 1.

This is an indication of an obvious lattice strain and charge transfer [34] that lead to a shift of d-band center of Pt-Pd SBCNCs versus Fermi level, and consequently to an enhancement of their catalytic properties [35]. The Pt-rich surface structure of Pt-Pd SBCNCs is further illustrated by XPS survey map in Fig. S4d, while the XPS patterns of Pt-Pd NCs are shown in Figs S4 (a, b and c). To further reveal the formation mechanism of Pt-Pd SBCNCs, a series of comparative experiments were designed and performed for the standard synthesis. First, we studied the role of halides in the proposed synthesis method by investigating the morphology of Pt-Pd bimetallic nanostructures at the effects of several different halide ions. When the synthesis was conducted in absence of I^- ions, maintaining the other conditions unchanged, we got an octahedral Pt-Pd nanostructure with uniform distribution and average

Table 1
The chemical composition and XPS data of three kinds of catalysts.

	Average particle sizes (nm)	Pt: Pd (by EDS)	Pt loading (μg cm^{-2})	Pt + Pd loading (μg cm^{-2})	Pt° $4f_{7/2}$ (eV)	Pt^{2+} $4f_{7/2}$ (eV)	Pt° $4f_{5/2}$ (eV)	Pt^{2+} $4f_{5/2}$ (eV)
TKK-Pt/C	3.2 ± 0.4	/	23.83	/	71.36	71.99	74.74	75.76
Pt-Pd NC	7.9 ± 1.2	28.3:71.7	12.02	24.26	71.43	72.29	74.82	75.49
Pt-Pd SBCNC	16.6 ± 2.4	32.4:67.6	11.40	26.04	71.54	72.71	74.93	76.21

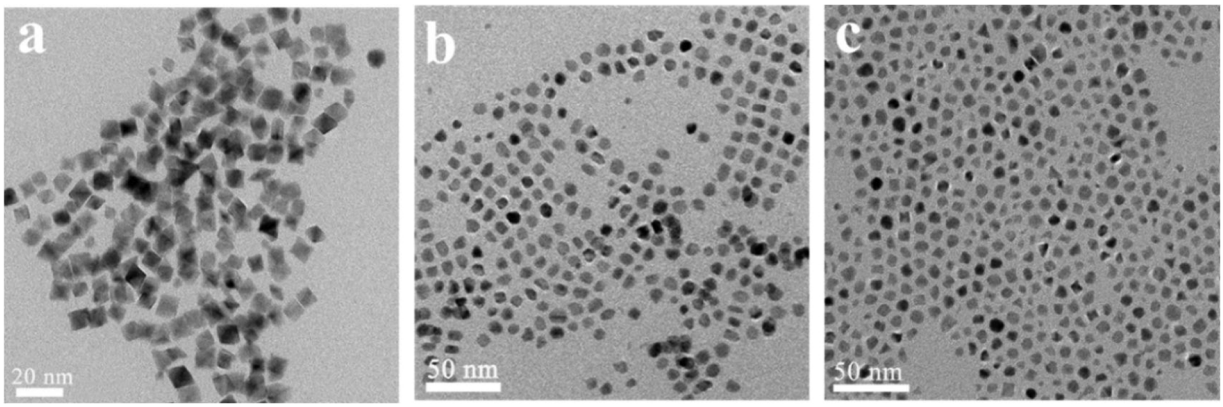

Fig. 3. Representative TEM images of Pt-Pd nanostructure prepared (a) in the absence of NaI; (b) and (c) replacing NaI with same molar amount of NaBr and NaCl, respectively.

particle size of 8.7 ± 2.6 nm (Figs 3a and S5).

Considering the use of H_2PtCl_6 and Na_2PdCl_4 as precursors, a small amount of Cl^-ions may be contained in the reaction solutions. When Pt (II) acetylacetonate and Pd(II) acetylacetonate were used as precursors, and in absence of halide ions, Pt-Pd nanoparticle with average size of 5.2 ± 0.9 nm were obtained; however, when added 40 mg NaI, the nanoparticles were transformed into concave nanocubes with an average size of 14.1 ± 1.1 nm (Fig. S6). This shows the importance of I^-ions for the formation of concave nanocube, regardless of whether the precursor is a platinum and palladium salt of a chloric or acetylacetonate. However, when we replace I^- with same molar amount Br^- ions, Pt-Pd nanocubes and a few irregular nanoparticles with an average edge length of 7.9 ± 1.2 nm were got [Figs 3b and S7(a, b)]. It is consistent with previous reports that Br^- ions serves as a capping agent selectively adsorbed on the (100) facet, facilitating the formation of nanocubes [7,33]. When I^- is replaced by Cl^-ions, the obtained Pt-Pd nanostructure also presents octahedral morphology and some irregular nanoparticles with an average edge length of 7.6 ± 1.5 nm [Figs 3c and S7(c, d)]. These observations are consistent with the suggested chemisorption order of halides on the metal surface as follows: $I^- > Br^- > Cl^-$ [36,37]. Interesting to be mentioned that when the amount of NaI is reduced to 20 mg or increased to 80 mg, the morphology of Pt-Pd SBCNCs have slightly changed when compared to the one with 40 mg NaI (Fig. S8). In conclusion, only the presence of I^- will inevitably lead to the formation of Pt-Pd SBCNCs.

We performed time-dependent experiments to further study the growth mechanism of the Pt-Pd SBCNCs and we investigated the intermediate products at different reaction time. At an initial growth period of 30 min, spherical nanoparticles, with an average size of 4.1 ± 0.6 nm were obtained (Figs 4a and S9a); the atomic ratio of Pt/Pd determined by the EDS analysis is found to be 6.4:93.6 (Figs S9b and S10).

When extending the reaction time to 60 min, the nanoparticles were evolved to nanocube with an average length of 8.9 ± 1.2 nm (Figs 4b and S9c); the atomic ratio of Pt/Pd is found to be 14.7:85.3 (Figs S9d and S10). When the reaction time was increased to 3 h, symmetry-broken concave nanocube with an average edge length of 13.8 ± 2.1 nm achieved (Figs 4c and S9e), and the atomic ratio of Pt/

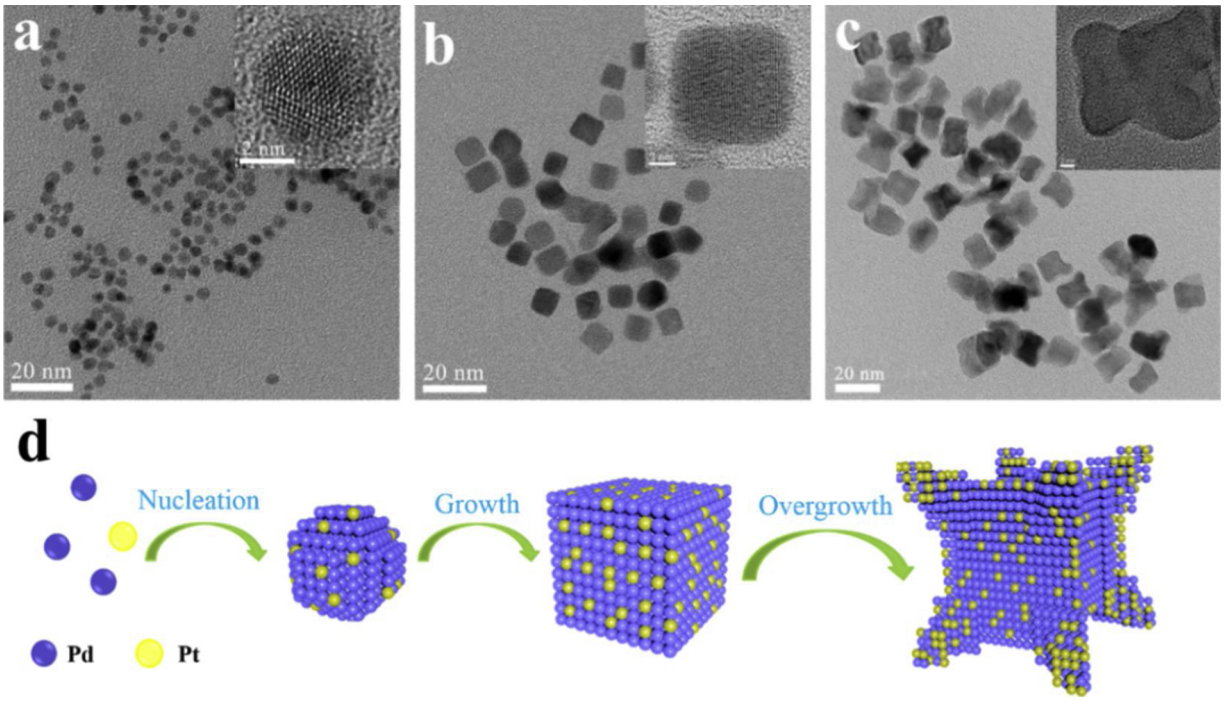

Fig. 4. TEM images of the Pt-Pd nanocrystals collected at (a) 0.5 h, (b) 1 h, and (c) 3 h of the reaction times, respectively. (d) Schematic illustration of the growth mechanism of Pt-Pd SBCNCs. The inset images of a, b, and c are corresponding HR-TEM images.

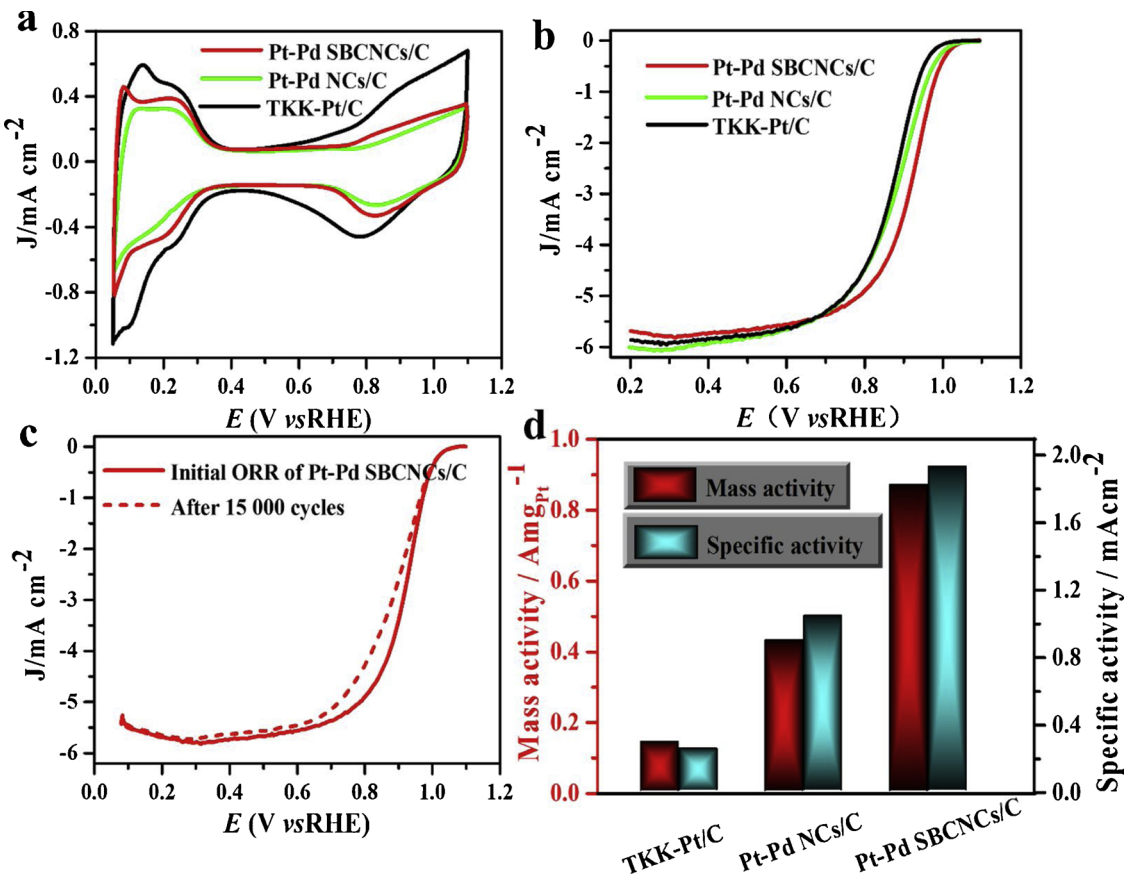

Fig. 5. (a) Cyclic voltammograms of commercial TKK-Pt/C, Pt-Pd NCs/C and Pt-Pd SBCNCs/C recorded at room temperature in an N_2-purged 0.1 M $HClO_4$ solution with a sweep rate of 50 mV s^{-1}. (b) Corresponding ORR polarization curves recorded in an O_2-saturated 0.1 M $HClO_4$ solution with a sweep rate of 10 mV s^{-1} and a rotation rate of 1600 rpm. (c) ORR polarization curves of the Pt-Pd SBCNCs/C catalyst before and after 15,000 potential cycles. (d) Histogram of specific and mass activities at 0.9 V versus RHE for three catalysts.

Pd is 28.2:71.8 (Figs S9f and S10). Finally, when the reaction time was increased to 5 h, a well-defined Pt-Pd SBCNCs structure (average length of 16.6 ± 2.4 nm and Pt-rich surface) with a noticeable variation in terms of symmetry and protrusion length of the corners for different nanocubes is obtained (Fig. S1).

According to the structural evolution process with reaction time continues, and in the previous report [13,30,38], we argued the growth mechanism of the Pt-Pd SBCNCs that most probably proceeds as shown in Fig. 4d. At the initial nucleation stage, since the effect of I^- ions, Pd nucleates and grows before Pt, and form a thermodynamically stable nanocrystal seed. By using the I^-ions in the reaction solution to passivate the {100} facets, nanocrystals will grow along the < 111 > directions and finally evolving to nanocube.

In addition, owing to the suppressive effect of no stirring during the reaction process, it is expected that Pt-Pd nanocube to pile-up of new atoms along the edge and/or over the vertexes, leading to the formation the Pt-Pd SBCNCs with Pt-rich surface structure.

To have a better understanding of the mechanism of the as proposed synthesis of Pt-Pd SBCNCs, we further explored the role of PVP (Poly (vinylpyrrolidone). As it can be distinguished from the TEM image shown in Fig. S11a, a severely aggregated nanostructure without specific morphology was obtained when the reaction was conducted in the absence of PVP. When added 25 or 100 mg PVP into the reaction solution, both of the nanocrystals show concave nanocubes structure, show slight changes at the surface morphology when compared with 50 mg of PVP were used in the standard synthesis procedure [Figs S11 (b, c and d)].

The electro-catalytic properties of the as-prepared Pt-Pd SBCNCs were evaluated by the aid of the reaction of oxygen reduction (ORR), and by benchmarking against Pt-Pd NCs and commercial Pt/C (46.7% Pt, TKK Japan) catalysts, adopting the commonly used test protocol. Before the electrochemical tests, the carbon-supported Pt-Pd SBCNCs (Pt-Pd SBCNCs/C) and Pt-Pd NCs (Pt-Pd NCs/C) were prepared by supporting Pt-Pd SBCNCs and Pt-Pd NCs on commercial carbon.

Fig. 5a shows cyclic voltammograms (CVs) of the Pt-Pd SBCNCs, of the Pt-Pd NCs and of the commercial Pt/C catalyst, recorded at 25°C in N_2-purged 0.1 M $HClO_4$ aqueous solution with ascan rate of 50 mV/s. The electrochemically active surface areas (ECSAs) were calculated based on charges involved in the adsorption of hydrogen. As seen from Fig. S12, ECSAs are 45.2, 37.4 and 52.7 $m^2 g_{Pt}^{-1}$ for Pt-Pd SBCNCs/C, for Pt-Pd NCs/C and for commercial Pt/C, summarized in Table 2. The ORR polarization curves for the different electrocatalysts are shown in Fig. 5b. The Pt loading for Pt-Pd SBCNCs/C, Pt-Pd NCs/C and the commercial Pt/C catalyst (TKK, 46.7 wt % Pt, Japan) are determined at 11.40, 12.02 and 23.83 μg cm^{-2}, respectively. In addition, the Pt + Pd loading for Pt-Pd SBCNCs/C and Pt-Pd NCs/C are 24.26 and 26.04 μg cm^{-2}, respectively (as shown in Table 1). It is based on the geometric electrode area of 0.196 cm^2 and determined by inductively coupled plasma mass spectroscopy measurements (ICP-MS). The ORR performance of three kinds of catalysts are shown in the Table 2.

In order to better understand the mass and surface effects, the kinetic currents of a polarization curve were calculated by the aid of Koutecky–Levich equation, and then normalized against the Pt mass and ECSA to get the mass and specific activities ($j_{k,\ mass}$ and $j_{k,\ specific}$), respectively (Fig. 5d). Pt-Pd NCs/C catalyst present 0.43 A mg_{Pt}^{-1} and 1.04 mA cm^{-2} toward mass activity and specific activity, respectively. Specially, the Pt-Pd SBCNCs/C exhibited a mass activity of 0.87 A mg_{Pt}^{-1}, and specific activity of 1.93 mA cm^{-2}, which are 6.2- and 7.7-

Table 2
ORR performances of three kinds of catalysts.

	ECSA ($m^2 g_{Pt}^{-1}$)	MA $^{0.9\ V}$ (A mg_{Pt}^{-1})	MA $^{0.9\ V}$ (A mg_{Pt+Pd}^{-1})	SA $^{0.9\ V}$ (mA cm_{Pt}^{-2})	MA $^{0.9\ V}$ (A mg_{Pt}^{-1}) after ADTs	SA $^{0.9\ V}$ (mA cm_{Pt}^{-2}) after ADTs
TKK-Pt/C	52.7	0.14	/	0.25	0.08	0.17
Pt-Pd NC	37.4	0.43	0.18	1.04	0.32	0.92
Pt-Pd SBCNC	45.2	0.87	0.48	1.93	0.47	1.12

fold enhancements compared with the commercial Pt/C catalyst (0.14 A mg_{Pt}^{-1} and 0.25 mA cm^{-2}), respectively. The mass activity of Pt-Pd NCs/C and Pt-Pd SBCNCs/C normalized with Pt + Pd loading amounts are 0.18 A mg_{Pt+Pd}^{-1} and 0.48 A mg_{Pt+Pd}^{-1}, respectively.

The enhanced performance is ascribed to the abundant high-index facets and a Pt-rich surface exposed on the Pt-Pd SBCNCs surface, and the synergistic effect between Pt and Pd is also essential to improve the activity of the catalyst [39]. In addition to the enhanced activity, the Pt-Pd SBCNCs/C also exhibited remarkable durability in an accelerated durability test (ADT) between 0.6 and 1.1 V (*vs.* RHE) (Fig. 5**c**) (at sweep rates of 100 mV s^{-1} in oxygen-saturated $HClO_4$ electrolyte). After 15 000 potential cycles, the Pt-Pd SBCNCs/C catalyst half-wave potential is reduced by only 30 mV, and the CV curves areas slightly shorter than the initial at the same condition, it still present 0.47 A mg_{Pt}^{-1} of mass activity and 1.12 mA cm^{-2} of specific activity. After durability tests, the structures of Pt-Pd SBCNCs were slightly changed. They still have various high-index facets at the surface of concave structure. The XPS analysis shows that the Pt 4f and Pd 3d spectra of Pt-Pd SBCNCs was very similar before and after stability tests (Fig. S14). The CV curves of Pt-Pd NCs/C and TKK-Pt/C catalysts after ADTs are shown in Fig. S13. The mass activity and specific activity of three catalysts after ADTs are summarized in Table 2.

4. Conclusions

In summary, we successfully reported a simple, cost-effective Pt-Pd SBCNCs catalysts were synthesized in a one-pot method. A series of contrast experiment was conducted to investigating the formation mechanism, and we found the presence of I^- ions and PVP play a key role in shaping the symmetry-broken concave nanocube. Through the analysis of TEM (mapping and line scan profile), XRD and XPS, we have proved that Pt-Pd bimetallic alloys and Pt-rich surface structure. Strikingly, electrochemical tests show that Pt-Pd SBCNCs exhibit superior catalytic activity and long-term durability, due to the high-index facet exposed on the Pt-rich surface and the synergistic effect between Pt and Pd. This work might provide us an attractive strategy for designing catalysts with a simple route, lower cost and remarkable catalytic activity and durability toward oxygen reduction reaction or other practical applications.

Acknowledgements

This work was supported by the Guangxi Science and Technology Project (AA17204083, AB16380030), National Basic Research Program of China (2015CB932304), the link project of the National Natural Science Foundation of China and Fujian Province (U1705252), the Natural Science Foundation of Guangdong Province (2015A030312007) and the Danish project of Initiative toward Non-precious Metal Polymer Fuel Cells (4106-000012B). The research of Prof. Tsiakaras was co-financed by the European Union and Greek national funds through the Operational Program Competitiveness, Entrepreneurship and Innovation, under the call RESEARCH–CREATE–INNOVATE (project code: T1EDK-02442).

Appendix A. Supplementary data

Supplementary material related to this article can be found, in the online version, at doi:https://doi.org/10.1016/j.apcatb.2019.03.045.

References

[1] M.K. Debe, Electrocatalyst approaches and challenges for automotive fuel cells, Nature 486 (2012) 43–51.
[2] A.M. Dafalla, F. Jiang, Stresses and their impacts on proton exchange membrane fuel cells: a review, Int. J. Hydrogen Energy 43 (2018) 2327–2348.
[3] N.V. Long, Y. Yang, C. Minh Thi, N.V. Minh, Y. Cao, M. Nogami, The development of mixture, alloy, and core-shell nanocatalysts with nanomaterial supports for energy conversion in low-temperature fuel cells, Nano Energy 2 (2013) 636–676.
[4] H.A. Gasteiger, S.S. Kocha, B. Sompalli, F.T. Wagner, Activity benchmarks and requirements for Pt, Pt-alloy, and non-Pt oxygen reduction catalysts for PEMFCs, Appl. Catal. B Environ. 56 (2005) 9–35.
[5] S. Chen, Z. Niu, C. Xie, M. Gao, M. Lai, M. Li, P. Yang, The effects of catalyst processing on the activity and stability of Pt-Ni nanoframe electrocatalysts, ACS Nano 12 (2018) 8697–8705.
[6] L. Bu, S. Guo, X. Zhang, X. Shen, D. Su, G. Lu, X. Zhu, J. Yao, J. Guo, X. Huang, Surface engineering of hierarchical platinum-cobalt nanowires for efficient electrocatalysis, Nat. Commun. 7 (2016) 11850.
[7] Y. Qi, T. Bian, S.I. Choi, Y. Jiang, C. Jin, M. Fu, H. Zhang, D. Yang, Kinetically controlled synthesis of Pt-Cu alloy concave nanocubes with high-index facets for methanol electro-oxidation, Chem. Commun. 50 (2014) 560–562.
[8] J. Wu, S. Shan, H. Cronk, F. Chang, H. Kareem, Y. Zhao, J. Luo, V. Petkov, C.-J. Zhong, Understanding composition-dependent synergy of PtPd alloy nanoparticles in electrocatalytic oxygen reduction reaction, J. Phys. Chem. C 121 (2017) 14128–14136.
[9] J. Ryu, J. Choi, D.-H. Lim, H.-L. Seo, S.-Y. Lee, Y. Sohn, J.H. Park, J.H. Jang, H.-J. Kim, S.A. Hong, P. Kim, S.J. Yoo, Morphology-controlled synthesis of ternary Pt–Pd–Cu alloy nanoparticles for efficient electrocatalytic oxygen reduction reactions, Appl. Catal. B Environ. 174–175 (2015) 526–532.
[10] C.V. Tinoco-Muñoz, J.L. Reyes-Rodríguez, D. Bahena-Uribe, M.A. Leyva, J.G. Cabañas-Moreno, O. Solorza-Feria, Preparation, characterization and electrochemical evaluation of Ni–Pd and Ni–Pd–Pt nanoparticles for the oxygen reduction reaction, Int. J. Hydrogen Energy 41 (2016) 23272–23280.
[11] X. Wang, S.I. Choi, L.T. Roling, M. Luo, C. Ma, L. Zhang, M. Chi, J. Liu, Z. Xie, J.A. Herron, M. Mavrikakis, Y. Xia, Palladium-platinum core-shell icosahedra with substantially enhanced activity and durability towards oxygen reduction, Nat. Commun. 6 (2015) 7594-7561.
[12] Z. Chen, M. Waje, W. Li, Y. Yan, Supportless Pt and PtPd nanotubes as electrocatalysts for oxygen-reduction reactions, Angew. Chem. Int. Ed. 46 (2007) 4060–4063.
[13] H. Zhang, M. Jin, J. Wang, W. Li, P.H. Camargo, M.J. Kim, D. Yang, Z. Xie, Y. Xia, Synthesis of Pd-Pt bimetallic nanocrystals with a concave structure through a bromide-induced galvanic replacement reaction, J. Am. Chem. Soc. 133 (2011) 6078–6089.
[14] J. Hong, S. WookKang, B.-S. Choi, D. Kim, S.B. Lee, SangWooHan, Controlled synthesis of Pd–Pt alloy hollow nanostructures with enhanced catalytic activities for oxygen reduction, ACS Nano 6 (2012) 2410–2419.
[15] L. Wang, Y. Yamauchi, Metallic nanocages: synthesis of bimetallic Pt-Pd hollow nanoparticles with dendritic shells by selective chemical etching, J. Am. Chem. Soc. 135 (2013) 16762–16765.
[16] X.-X. Lin, A.-J. Wang, K.-M. Fang, J. Yuan, J.-J. Feng, One-pot seedless aqueous synthesis of reduced graphene oxide (rGO)-supported core–shell Pt@Pd nanoflowers as advanced catalysts for oxygen reduction and hydrogen evolution, ACS Sustain. Chem. Eng. 5 (2017) 8675–8683.
[17] N. Tian, Z.-Y. Zhou, N.-F. Yu, L.-Y. Wang, S.-G. Sun, Direct electrodeposition of tetrahexahedral Pd nanocrystals with high-index facets and high catalytic activity for ethanol electrooxidation, J. Am. Chem. Soc. 132 (2010) 7580–7581.
[18] S. Luo, M. Tang, P.K. Shen, S. Ye, Atomic-scale preparation of octopod nanoframes with high-index facets as highly active and stable catalysts, Adv. Mater. 29 (2017) 1601687.
[19] Z. Quan, Y. Wang, J. Fang, High-index faceted noble metal nanocrystals, Acc. Chem. Res. 46 (2013) 191–202.
[20] S.E. Habas, H. Lee, V. Radmilovic, G.A. Somorjai, P. Yang, Shaping binary metal nanocrystals through epitaxial seeded growth, Nat. Mater. 6 (2007) 692–697.
[21] Y. Xia, K.D. Gilroy, H.C. Peng, X. Xia, Seed-mediated growth of colloidal metal nanocrystals, Angew. Chem. Int. Ed. 56 (2017) 60–95.
[22] Y. Zheng, J. Qiao, J. Yuan, J. Shen, A.-j. Wang, S. Huang, Controllable synthesis of PtPd nanocubes on graphene as advanced catalysts for ethanol oxidation, Int. J. Hydrogen Energy 43 (2018) 4902–4911.
[23] J.-J. Lv, J.-N. Zheng, L.-L. Chen, M. Lin, A.-J. Wang, J.-R. Chen, J.-J. Feng, Facile synthesis of bimetallic alloyed Pt-Pd nanocubes on reduced graphene oxide with enhanced eletrocatalytic properties, Electrochim. Acta 143 (2014) 36–43.
[24] F. Zhan, T. Bian, W. Zhao, H. Zhang, M. Jin, D. Yang, Facile synthesis of Pd–Pt alloy concave nanocubes with high-index facets as electrocatalysts for methanol

oxidation, CrystEngComm 16 (2014) 2411–2416.
[25] R. Zhang, C.L. Sun, Y.J. Lu, W. Chen, Graphene nanoribbon-supported PtPd concave nanocubes for electrochemical detection of TNT with high sensitivity and selectivity, Anal. Chem. 87 (2015) 12262–12269.
[26] Y. Lu, Y. Jiang, W. Chen, Graphene nanosheet-tailored PtPd concave nanocubes with enhanced electrocatalytic activity and durability for methanol oxidation, Nanoscale 6 (2014) 3309–3315.
[27] X. Huang, H. Zhang, C. Guo, Z. Zhou, N. Zheng, Simplifying the creation of hollow metallic nanostructures: one-pot synthesis of hollow palladium/platinum single-crystalline nanocubes, Angew. Chem. Int. Ed. 48 (2009) 4808–4812.
[28] P.J. Straney, L.E. Marbella, C.M. Andolina, N.T. Nuhfer, J.E. Millstone, Decoupling mechanisms of platinum deposition on colloidal gold nanoparticle substrates, J. Am. Chem. Soc. 136 (2014) 7873–7876.
[29] J. Zhang, L. Wan, L. Liu, Y. Deng, C. Zhong, W. Hu, PdPt bimetallic nanoparticles enabled by shape control with halide ions and their enhanced catalytic activities, Nanoscale 8 (2016) 3962–3972.
[30] M. Vara, Y. Xia, Facile synthesis of Pd concave nanocubes: from kinetics to mechanistic understanding and rationally designed protocol, Nano Res. 11 (2018) 3122–3131.
[31] N. Tian, Z.-Y. Zhou, S.-G. Sun, Y. Ding, Z.L. Wang, Synthesis of tetrahexahedral platinum nanocrystals with high-index facets and high electro-oxidation activity, Science 316 (2007) 732–735.
[32] J. Zhang, M.R. Langille, M.L. Personick, K. Zhang, S. Li, C.A. Mirkin, Concave cubic gold nanocrystals with high-index facets, J. Am. Chem. Soc. 132 (2010) 14012–14014.
[33] T. Yu, D.Y. Kim, H. Zhang, Y. Xia, Platinum concave nanocubes with high-index facets and their enhanced activity for oxygen reduction reaction, Angew. Chem. Int. Ed. 123 (2011) 2825–2829.
[34] J.N. Tiwari, W.G. Lee, S. Sultan, M. Yousuf, A.M. Harzandi, V. Vij, K.S. Kim, High-affinity-assisted nanoscale alloys as remarkable bifunctional catalyst for alcohol oxidation and oxygen reduction reactions, ACS Nano 11 (2017) 7729–7735.
[35] V.R. Stamenkovic, B.S. Mun, K.J.J. Mayrhofer, P.N. Ross, N.M. Markovic, Effect of surface composition on electronic structure, stability, and electrocatalytic properties of Pt-Transition metal alloys_ Pt-Skin versus Pt-skeleton surfaces, J. Am. Chem. Soc. 128 (2006) 8813–8819.
[36] A. Carrasquillo, J.J. Jeng, R.J. Barriga, W.F. Temesghen, M.P. Soriaga, Electrode-surface coordination chemistry: ligand substitution and competitive coordination of halides at well-defined Pd(100) and Pd(111) single crystals, Inorganica Chim. Acta 255 (1997) 249–254.
[37] M.P. Soriaga, J.A. Schimpf, J.A. Carrasquillo, J.B. Abre, W. Temesghen, R.J. Barriga, jj. Jeng, K. Sashikata, K. Itaya, Electrochemistry of the I-on-Pd single-crystal interface: studies by UHV-EC and in situ STM, Surf. Sci. 335 (1995) 273–280.
[38] H. Lee, S.E. Habas, G.A. Somorjai, P. Yang, Localized Pd overgrowth on cubic Pt nanocrystals for enhanced electrocatalytic oxidation of formic acid, J. Am. Chem. Soc. 130 (2008) 5406–5407.
[39] Y.-J. Deng, N. Tian, Z.-Y. Zhou, R. Huang, Z.-L. Liu, J. Xiao, S.-G. Sun, Alloy tetrahexahedral Pd–Pt catalysts: enhancing significantly the catalytic activity by synergy effect of high-index facets and electronic structure, Chem. Sci. 3 (2012) 1157–1161.